

Validated numerical analysis of vortical structures in 3D AC electro-osmotic flows

Zhipeng Liu · Michel F. M. Speetjens ·
Arjan J. H. Frijns · Anton A. van Steenhoven

Received: 27 March 2013 / Accepted: 31 October 2013 / Published online: 8 March 2014
© Springer-Verlag Berlin Heidelberg 2014

Abstract This paper presented an experimental validation of a numerical study on the vortical structures in AC electro-osmotic (ACEO) flows. First, the 3D velocity field of ACEO vortices above the symmetric electrodes was experimentally investigated using astigmatism microparticle tracking velocimetry. The experimentally obtained velocities were used to validate an extended nonlinear Gouy–Chapman–Stern model accounting for the surface conduction effect. A qualitative agreement between the simulations and experiments was found for the velocity field when changing AC voltage (from 0.5 to 2 V) and the frequency (from 50 to 3,000 Hz). However, the predicted magnitude of the velocity profiles was much higher than the experimentally obtained ones, except in some cases at low frequency. For frequencies higher than 200 Hz, a correction factor was introduced to make the numerical results quantitatively comparable to the experimental ones. In addition, the primary circulation, given in terms of the spanwise component of vorticity, was numerically and experimentally analyzed as function of frequency and amplitude of the AC voltage. The outline of the vortex boundary was determined via the eigenvalues of the strain-rate tensor estimated from the velocity field. It revealed that the experimental circulation was frequency dependent, tending to zero at both low and high frequency and the maximum changing from around 600 Hz for 1 V to 300 Hz for 2 V. The variation in the predicted vortex circulation as function of frequency and voltage, after using the above correction factor, was in good correspondence with

the experiments. These results yield first insights into the characteristics of 3D ACEO flows and the ability of current numerical models to adequately describe them.

Keywords 3D velocity measurement · Numerical modeling · AC electro-osmosis · Microflows

1 Introduction

AC electro-osmosis is in essence flow forcing by electrokinetic effects induced via a low-voltage AC electric field (Ramos et al. 1998). Unidirectional motion of the mobile charge carriers (ions) accumulated in the electric double layer (EDL) gives rise to a slip layer that acts as a 'driving wall' above the electrode surface, directed from the electrode edge to its center (Ramos et al. 1999). This slip velocity is strongly determined by the ion dynamics and the gradient of the electric field in the EDL, and reaches a maximum nearby the electrode edge. The velocity magnitude can be characterized in terms of the frequency and amplitude of the applied AC voltage and the electrolyte conductivity. It tends to zero at both low and high frequencies, and depends nonlinearly on the amplitude of the voltage (Green et al. 2000). However, so far experimental observations and numerical simulations exhibit great discrepancies, and the results vary with the properties of the fluids (Green et al. 2002; Bazant et al. 2009). Several aspects of ACEO flow are still not fully understood. In-depth experimental and numerical investigations of the 2D and 3D velocity distributions are an essential step in further exploring ACEO as a flow-forcing technique in lab-on-a-chip systems.

Proper modeling of ACEO remains a formidable challenge to date and then in particular for higher AC voltages. In theory, the behavior of aqueous suspensions of charge ions

Z. Liu · M. F. M. Speetjens · A. J. H. Frijns (✉) ·
A. A. van Steenhoven
Department of Mechanical Engineering, Eindhoven University
of Technology, P.O. Box 513, 5600 MB Eindhoven,
The Netherlands
e-mail: a.j.h.frijns@tue.nl

under the action of AC electric fields relates to the structure and electric state of its ionic atmosphere (EDL) and solid/liquid interface (Lyklema 1995). According to the classical Poisson–Boltzmann theory, the distribution of the ion density q in a binary symmetric electrolyte subject to an electric field (e.g., an aqueous solution of salt containing an equal number of positive and negative ions with equal mobilities) is a function of the potential drop across the diffuse layer of the EDL (the so-called zeta potential, ζ) according to the relation (Morgan and Green 2002; Olesen et al. 2006),

$$q = -\frac{\varepsilon}{\lambda_D} \frac{2k_B T}{ze} \sinh\left(\frac{ze\zeta}{2k_B T}\right), \quad (1)$$

where ε is the permittivity of the solvent, k_B the Boltzmann's constant, T the temperature, $\lambda_D = \sqrt{\varepsilon k_B T / 2c_o z^2 e^2}$ the Debye length (c_o is the ionic concentration), e an elementary charge and z its valence. The bulk solution, i.e., the region outside the EDL, is assumed to be charge neutral with uniform charge concentration. Hence, (dis)charging of the electrolyte is considered to take place only in the diffuse layer. Moreover, the thickness of the EDL, given by the Debye length, is negligible compared with the typical dimensions of the flow domain and may thus be ignored; its effect upon the electric field in the domain interior is incorporated in nonlinear boundary conditions (Ajdari 2000; Ramos et al. 2003; Olesen et al. 2006). These assumptions reduce the electro-kinetic problem to the nonlinear Gouy–Chapman model. In order to resolve the shortcomings of the Gouy–Chapman model, an extension accounting for the Stern layer in series with the diffuse layer is incorporated, resulting in the Gouy–Chapman–Stern (GCS) model (Morgan and Green 2002). This GCS model is the most commonly used. In spite of predictions qualitatively similar to experiments (Bazant et al. 2009), the classical GCS model nonetheless tends to overpredict the fluid velocity at high voltages. Some phenomena which might take place at high voltages were taken into account by others, including Faradaic current injection (Olesen et al. 2006) and steric effect of ions of finite size in the diffuse layer (Kilic et al. 2007; Storey et al. 2006). It was found that the production of ions by Faradaic reaction reduces the slip velocity significantly (Olesen et al. 2006). To fit the steric effects incorporated in the model to experimental data, the ion size has to be about one order of magnitude larger than their physical values (Storey et al. 2006).

Surface conduction refers to the movement of charged ions within the EDL (Lyklema 1995). As the ionic concentration increases exponentially with respect to the zeta potential, $q \propto \sinh(ze\zeta/2k_B T)$, the conductivity of the electrolyte in the EDL due to excess ions might be much higher than in the bulk at high voltages. As a result, a

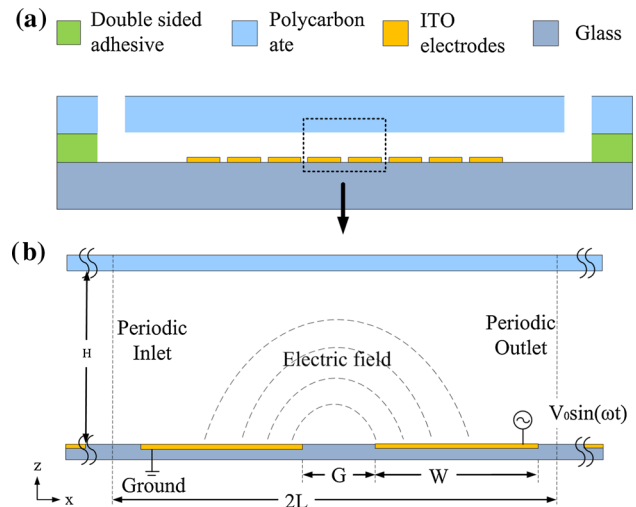


Fig. 1 Schematic diagram of the microchannel with a symmetric periodic electrode array. **a** The structure of the channel, **b** ACEO configuration of a 2D periodic microchannel with a symmetric electrode pair, which encompasses the horizontal extent $L = W + G$, with W and G indicating the electrode and gap widths, respectively

significant amount of ion flux parallel to the surface through the EDL reduces the tangential component of the electric field, leading to lowering the ACEO velocity (Soni et al. 2007; Khair and Squires 2008; Gregersen et al. 2009). The present study aims to investigate whether the extended model accounting for surface conduction provides a better prediction of experimental observations.

In this paper, we present a numerical investigation of the experimentally measured 3D flow structure of AC electroosmosis. By way of 3D velocity measurements using astigmatism microparticle tracking velocimetry (astigmatism μ -PTV) (Cierpka et al. 2010), presence and properties of flow structures are obtained in laboratory experiments. Simulations of ACEO flow are performed with an extended nonlinear GCS model accounting for the surface conduction. Compared with the standard GCS model, the effect of surface conduction on the predicted slip velocity is analyzed. Its predictions are qualitatively validated by these experimental results. Due to the over-prediction by the model, a global correction factor for the velocity is proposed to compare the numerical to the experimental results. The experimental and numerical fields after this correction are then compared.

2 Experimental setup and measurement

2.1 Laboratory setup

The microfluidic device consists of a straight microchannel, which was made by bounding a double-sided adhesive acrylic type sheet (Optically Clear Adhesive 8212, 3MTM,

USA) between a polycarbonate top layer (0.5 mm thick) and glass substrate layer (0.7 mm thick), shown schematically in Fig. 1a. On top of the glass substrate, an indium tin oxide (ITO) layer with 120 nm thickness (Prazisions Glas & Optik GmbH, Germany) was deposited as electrode. The symmetric parallel electrode pattern was fabricated by using photolithography (Liu et al. 2013) and is perpendicular with respect to the axial direction of the channel. The width of each electrode is $W = 56 \mu\text{m}$, and the gap between the electrodes is $G = 14 \mu\text{m}$. Correspondingly, one spatial period encompasses the horizontal extent $L = W + G$, as shown in Fig. 1b. In the acrylic type sheet, the outline of the microchannel is formed by ablation with an Excimer-laser (Micromaster, OPTEC Co., Belgium). The whole channel is about $H = 48 \mu\text{m}$ high and 1 mm wide.

The device was mounted on a chip holder and was connected via a silicon tube with an inner diameter of 0.79 mm (L/S, Masterflex, the Netherlands) to a syringe. Potassium chloride (KCl) solutions with a concentration of 0.1 mM (Sigma-Aldrich Co., USA) were used as working fluid. Fluorescent polymer microparticles with a diameter of $d_p = 2 \mu\text{m}$ (Fluoro-Max, Duke Scientific Corp., Canada, 1 % solids, with a density of 1.05 g/cm^3) were utilized as tracer particles to measure fluid velocity and were diluted in the working fluid with a concentration of about 0.01 % particle–solution volume. In order to accurately evaluate the particle image in the image-processing procedure, the signal-to-noise ratio (SNR) of image should be as high as possible (Cierpka et al. 2010). In a previous study (Liu et al. 2013), it was found that when using tracer particles with a diameter of $2 \mu\text{m}$, the SNR was high enough that such the algorithm gives reliable results, and when reducing the diameter of the tracer particle to about $1 \mu\text{m}$, the SNR was significantly reduced, leading to the measurement uncertainty to become unacceptable.

The electric conductivity of the working fluid with tracer particles was measured to be $\sigma = 1.7 \text{ mS/m}$ (IQ170, Scientific Instruments, USA). In the experiments, the channel was filled with the solution and subsequently closed. A function generator (Sefram4422, Sefram, the Netherlands) provides an AC signal to the electrode arrays. Its potential and frequency were measured by a digital oscilloscope (TDS210, Tektronix, USA). The particle movement was observed using a fluorescence microscope with a $20\times$ Zeiss objective lens. The Nd:YAG laser generation (ICE450, Quantel, USA) produces a pulsed monochromatic laser beam with a wavelength of 532 nm. The light of the illuminated tracer particles has a wavelength of 612 nm. Images of these tracer particles were recorded by a digital camera (12-bit SensiCam qe, PCO, Germany). The successive images were recorded in alternating time delays, 0.03 and 0.37 s. A digital delay generator (DG535, Stanford Research Systems, USA) controls the timing of the laser and camera simultaneously.

2.2 Velocity measurement

The measurement procedure is based on the astigmatism μ -PTV (Chen et al. 2009; Cierpka et al. 2010, 2010). The basic principle is that due to a cylindrical lens added in the optical access, the particles images are deformed into ellipses. As this ellipticity is directly related to the particle position normal to the focal plane, one can identify the particle position in the measurement domain by examining the defocus of the wavefront scattered by a particle and thus establish the three components of the velocity field. In our setup, a cylindrical lens with a focal length of 150 mm was used. Based on the calibration function, the three-dimensional positions of tracer particles were estimated. Due to the refractive effect, the apparent z -position needed to be corrected by multiplying with the refractive index of water ($n_{\text{water}} = 1.33$) (Liu et al. 2013). The standard deviation on z -position of the measured particles across the field of view was less than $0.7 \mu\text{m}$.

In the present experiments, the tracer particles are mainly subject to the ACEO flow and dielectrophoresis force (DEP) (Castellanos et al. 2003). Assuming that the movement of particles is only due to DEP forces, the particle velocity is described by

$$u_{\text{DEP}} = \frac{d_p^2 \varepsilon \text{Re}(\chi_{\text{CM}}) \nabla |E_{\text{RMS}}|^2}{12\mu}, \quad (2)$$

where μ is the dynamic viscosity of the bulk solution, $\nabla |E_{\text{RMS}}|^2$ the gradient of the square of the RMS electric field and $\text{Re}(\chi_{\text{CM}})$ the real part of the Clausius–Mossotti (CM) factor (Castellanos et al. 2003). For a polystyrene particle with a conductivity of 10 mS/m and permittivity of $2.55\varepsilon_0$ (ε_0 the absolute permittivity of vacuum) in the suspending medium with a conductivity of $\sigma = 1.7 \text{ mS/m}$ and permittivity of $\varepsilon = 78\varepsilon_0$, $\text{Re}(\chi_{\text{CM}})$ is about 0.62 for the frequencies much less than the crossover frequency ($\sim 10^6 \text{ Hz}$) (Green and Morgan 1999). Assuming the electric field is semi-circular as in Castellanos et al. (2003), and Kim et al. (2009), one can obtain $E_{\text{RMS}} = V_d / \sqrt{2}\pi r$ for symmetric electrodes, where r is the distance to the center of the gap and V_d the potential difference applied in the bulk solution. The particle velocity due to the DEP is then simplified to

$$u_{\text{DEP}} = \frac{d_p^2 \varepsilon \text{Re}(\chi_{\text{CM}}) V_d^2}{12\mu\pi^2 r^3}. \quad (3)$$

In general, V_d in bulk is much lower than the voltage difference applied between the electrodes due to the charging of the EDL. Assuming V_d is half of the voltage difference applied on the electrodes, u_{DEP} is maximum at the electrode edges ($r = 7\mu\text{m}$) and is about 2.6, 10.5, 23.6 and $42.2 \mu\text{m/s}$ at applied voltage of 0.5, 1, 1.5 and 2 V, respectively.

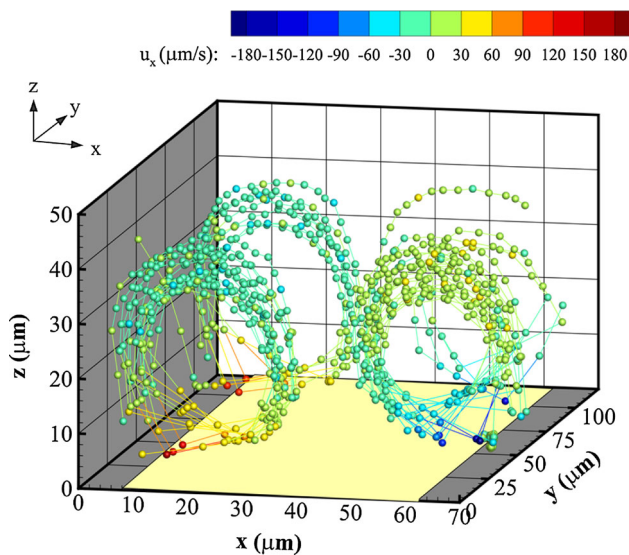


Fig. 2 3D trajectories of several particles measured at applied frequency of 1,000 Hz and voltage of 1 V, where the *yellow area* indicates the position of the electrode (color figure online)

Compared with the measured ACEO velocities close to the electrode edges, which values are around 20, 80, 170 and 320 $\mu\text{m/s}$ for frequencies from 50 to 3,000 Hz at voltages of 0.5, 1, 1.5 and 2 V respectively, u_{DEP} is about one order smaller. The above calculation is based on the comparison between the experimental absolute velocities and the modeled DEP velocities. In a study by Kim et al. (2009), the ratio of the estimated DEP velocities and the estimated ACEO velocities is considered. This leads to a frequency-dependent result, with a high influence of DEP at low frequencies ($f \lesssim 700$ Hz) and a low influence at higher frequencies. Furthermore, this DEP effect reduces rapidly: according to Eq. 3, it is inversely proportional with r^3 . Therefore, we may assume that close to electrode edges, the DEP forces have an influence on the measured values, but that for the average velocities along the whole electrode, its influence will be much less.

In order to minimize any possible influence from the channel walls on the flow field, the measurement view of astigmatism μ -PTV focuses in the center of the channel. Figure 2 depicts the 3D trajectories of several particles at a voltage of 1 V and a frequency of 1,000 Hz, where the time-ordered set of these trajectories has two alternating time delays (0.03 and 0.37 s).

According to the 3D positions (x , y and z) of the tracer particles in successive frames, one can calculate the three components of the particle velocity (u_x , u_y and u_z). As can be seen in Fig. 2, u_x varies from $-180 \mu\text{m/s}$ to $180 \mu\text{m/s}$ above the electrode surface. The positive and negative peaks of u_z are observed at the centers of the electrode surface and the gap, respectively. Contrary to u_x and u_z , the value of u_y remains small everywhere in the bulk flow,

meaning the particle can have a good approximation to be considered a quasi-2D flow, perpendicular to the electrode edge. In this case, the 3D velocity data are projected in the (x , z) plane, yielding a 2D velocity field. According to our previous study (Liu et al. 2013), the velocity field was found to be periodic over symmetric electrode pairs. All particle velocity vectors are then overlaid into one domain including one electrode. The quasi-2D velocity vectors of the particles show two symmetric counter-rotating vortices form above electrode surface.

For each case with fixed voltage and frequency, two data sets were obtained, corresponding to two time delays (0.03 and 0.37 s). Dependent to the measured velocity magnitude, one data set in one time delay is chosen to analyze the velocity field (the data set for time delay of 0.37 s can only be used when the maximum of the measured velocity is less than 57 $\mu\text{m/s}$). For a data set, around 12,000 particle velocity vectors were obtained. In the data post-processing procedure, error vectors due to sticking particles and mismatching of tracking particles were eliminated from the raw data set. To distinguish the sticking particles on the bottom wall, a discrimination process was performed based on the minimum displacement of the tracer particles at the distance less than 3 μm away from the bottom wall (Liu et al. 2013). After filtering out the sticking particles, the outlier filter was applied based on the global standard deviation $\sigma = \sqrt{\frac{1}{N} \sum_{i=1}^N e_i^2}$ with $e_i^2 = \mathbf{u}' \cdot \mathbf{u}'$, $\mathbf{u}'(\mathbf{x}_i, \mathbf{z}_i) = \mathbf{u}(\mathbf{x}_i, \mathbf{z}_i) - \bar{\mathbf{u}}(x_i, z_i)$ the local deviation and $\bar{\mathbf{u}}(x_i, z_i)$ the local average velocity at the position of individual particle (x_i, z_i). To calculate $\bar{\mathbf{u}}(x_i, z_i)$, the Gaussian averaging algorithm was utilized, where a weighting of the neighboring particles is determined by their distances and the Gaussian constant (0.5 μm) (Liu et al. 2013). As a result, the data points with $e_i > 2\sigma$ are removed from the data set. The retained particle velocity vectors were interpolated onto a regular Cartesian grid with an equidistant spacing $(\Delta x, \Delta z) = (1 \mu\text{m}, 1 \mu\text{m})$ in the (x , z) plane, by using a Gaussian averaging algorithm (Liu et al. 2013).

3 Numerical methods

3.1 Numerical models

In this study, numerical simulations of ACEO flow were carried out by using the nonlinear electro-kinetic model: the classical GCS model by accounting for the surface conduction. To this end, the EDL is assumed in a state of quasi-equilibrium ($\omega \ll \tau_{\text{EDL}}^{-1}$, with ω the oscillating angular frequency and $\tau_{\text{EDL}} = \varepsilon/\sigma$ being the relaxation time of the cyclic EDL charging), in which the relationship between the charge distribution and the potential is described as Poisson–

Boltzmann statistics. The bulk solution, apart from the EDL, is assumed to be charge neutral with a uniform charge concentration (Ramos et al. 2003; Olesen et al. 2006). To relate the surface conductivity to local concentrations and local species of ions, the electro-convection of ions in the EDL is considered (Lyklema 1995). Furthermore, the applied frequency ω is assumed to be so high that the fluid cannot follow the instantaneous changes in propagation direction of ions during each AC cycle; the fluid “feels” only the time-averaged slip velocity. According to the electrode pattern and the resulting velocity field in the experiment, a two-dimensional geometry shown in Fig. 1 is considered in the present model.

In the bulk domain ($0 \leq x \leq 2L$ and $0 \leq z \leq H$) the electric potential $\phi(x, z, t)$ is governed by the Laplace equation

$$\nabla^2 \phi = 0. \tag{4}$$

On the insulated channel wall, the normal current vanishes, and thus, the boundary condition of the bulk domain is described as

$$\sigma \frac{\partial \phi}{\partial z} = 0. \tag{5}$$

On the electrodes, the induced EDL acts as an ideal capacitor; its effect upon the electro-kinetics is represented by the charge conservation equation. Combined with the effect of the surface conduction, the dynamic charging of the EDL is defined (Soni et al. 2007; Gregersen et al. 2009) as

$$\frac{\partial q}{\partial t} = \sigma \frac{\partial \phi}{\partial z} - \frac{\partial}{\partial x} \mathbf{J}_T, \tag{6}$$

where $\mathbf{J}_T = \sigma_T \mathbf{E}_T = -\sigma_T \partial \phi / \partial x$ is the electric surface current density with σ_T the surface conductivity and \mathbf{E}_T the tangential electric field.

Full closure of model (4–6) requires a specification of the relation between $\phi(x, z, t)$ and $q(x, t)$. To this end, the potential drop across the double layer is given by (Ramos et al. 2003; Olesen et al. 2006)

$$V_{\text{ext}} - \phi = \zeta - \frac{q}{C_s}, \tag{7}$$

where leading and trailing term of the right-hand side correspond with the potential drops in the diffuse layer and Stern layer (with capacitance C_s), and $V_{\text{ext}} = V_o \sin(\omega t)$ represents AC voltage applied on the electrode (V_o voltage amplitude). The total capacitance of the double layer is defined as

$$C_{DL} = \left[\frac{1}{C_d} + \frac{1}{C_s} \right]^{-1} = \frac{1}{1 + \delta} C_d,$$

where C_d is the capacitance of diffuse layer, and $\delta = C_d/C_s$ is a capacitance ratio between diffuse layer and Stern layer. In the Debye–Hückel approximation, $C_d = \varepsilon/\lambda_D$, leading to $C_{DL} = \varepsilon/\lambda_D(1 + \delta)$ (Bazant et al. 2009; Olesen et al. 2006). By eliminating ζ through relation in Eqs. 1 and 7 is rewritten as (Olesen et al. 2006)

$$V_{\text{ext}} - \phi = -\frac{2k_B T}{ez} \sinh^{-1} \left(\frac{\lambda_D e z q}{2 \varepsilon k_B T} \right) - \frac{\delta \lambda_D q}{\varepsilon}, \tag{8}$$

which, together with relations (4–6), provides a fully closed nonlinear model for the bulk potential ϕ .

As the Reynolds number is usually very small for the typical microflow, the behavior of the fluid \mathbf{u} is governed by the steady Stokes equations (Ramos et al. 2003),

$$\nabla \cdot \mathbf{u} = 0, \quad -\nabla p + \mu \nabla^2 \mathbf{u} = \mathbf{0}, \tag{9}$$

with p the pressure. No-slip conditions are imposed on boundary segments other than the electrodes. The time-averaged slip velocity, given by the Helmholtz–Smoluchowski formula (Olesen et al. 2006)

$$\langle u_{\text{slip}} \rangle = \frac{\omega}{2\pi} \int_0^{2\pi/\omega} u_{\text{slip}} dt, \quad u_{\text{slip}} = -\frac{\varepsilon \zeta}{\mu} E_T = \frac{\varepsilon \zeta}{\mu} \frac{\partial \phi}{\partial x}, \tag{10}$$

is imposed upon the electrodes. Note that despite essentially unsteady electro-kinetics, we obtain a steady-state flow field as the fluid “feels” only the time-averaged slip velocity due to the high AC frequency. For inlet and outlet of the numerical domain, periodic boundary conditions are applied both for the electric and flow models.

According to the experimental situation, 0.1 mM KCl solution is considered to be the electrolyte in the simulation. $V_{\text{ext}} = V_o \sin(\omega t)$ is applied on one electrode while a ground potential $V_{\text{ext}} = 0$ is connected to the other (see Fig. 1). Considering the physical screening length ratio between the diffuse layer and the Stern layer (Bazant et al. 2009), $\delta = 0.1$ is chosen in this study. The constants used in the simulation are given in Table 1.

For simplicity of the analysis, the simulations were performed using dimensionless parameters. The electro-kinetic and flow models are nondimensionalized by rescaling the governing equations and relevant variables via

$$\begin{aligned} [\hat{x}, \hat{z}] &= \frac{[x, z]}{G}, \quad \hat{t} = \frac{t}{\tau_{RC}}, \quad \hat{\phi} = \frac{\phi}{\phi_o}, \quad \hat{q} = \frac{q}{\phi_o C_{DL}}, \\ \hat{\mathbf{u}} &= \frac{\mathbf{u}}{u_o}, \quad \hat{p} = \frac{p}{\rho \nu u_o / G}, \end{aligned} \tag{11}$$

with $\tau_{RC} = C_{DL} G / \sigma$ the equivalent electric circuit, $\phi_o = k_B T / ze$ the thermal potential and $u_o = \varepsilon V_o^2 / \mu G$ the natural

Table 1 Constants used in the simulations for a 0.1 mM KCl solution

	Value	Unit	Description
G	14	μm	Characteristic length
ε	6.943×10^{-10}	C^2/Nm^2	Permittivity
σ	1.7	mS/m	Electric conductivity
D	1.98×10^{-9}	m^2/s	Diffusion coefficient of ions
μ	1×10^{-3}	Pa s	Viscosity
z	1	–	Valence of ions
c_o	0.1	mM	ionic concentration (completely diluted)
m	0.45	–	Ratio between ion electro-convection to migration
δ	0.1	–	Capacitance ratio
λ_D	30	nm	Debye length ($c_o = 0.1 \text{ mM}$)
T	293.15	K	Temperature

scale of the slip velocity (Olesen et al. 2006). Accents indicate dimensionless variables. Therefore, the dimensionless governing equation of electrical potential (Eq. 4) is

$$\hat{\nabla}^2 \hat{\phi} = 0. \quad (12)$$

The boundary condition on the insulating walls is

$$\frac{\partial \hat{\phi}}{\partial \hat{z}} = 0. \quad (13)$$

On the electrodes, the boundary condition is given as

$$\frac{\partial \hat{q}}{\partial \hat{t}} = \frac{\partial \hat{\phi}}{\partial \hat{z}} + \frac{\partial}{\partial \hat{x}} \left(Du \frac{\partial \hat{\phi}}{\partial \hat{x}} \right), \quad (14)$$

where $Du = \sigma_T / G\sigma$ is the Dukhin (Du) number (Lyklema 1995). For a binary symmetrical electrolyte with identical diffusion coefficients D , the Du number simplifies to (Lyklema 1995; Soni et al. 2007; Gregersen et al. 2009)

$$Du = \frac{4\lambda_D}{G} (1+m) \sinh^2 \left(\frac{ze\zeta}{4k_B T} \right), \quad (15)$$

with $m = 2\varepsilon(k_B T/e)^2 / \mu D$ the ratio between ion electro-convection to the electro-migration (Lyklema 1995).

The dimensionless potential distribution across the double layer is written as

$$\hat{V}_{\text{ext}} - \hat{\phi} = 2 \sinh^{-1} \left(-\frac{\hat{q}}{2(1+\delta)} \right) - \frac{\hat{q}\delta}{(1+\delta)}. \quad (16)$$

with $\hat{V}_{\text{ext}} = \hat{V}_o \sin(\hat{\omega}t)$ and $\hat{V}_{\text{ext}} = 0$ on the electrode pair.

The nondimensional form of the steady Stokes equations is then written as

$$\hat{\nabla} \cdot \hat{\mathbf{u}} = 0, \quad -\hat{\nabla} \hat{p} + \hat{\nabla}^2 \hat{\mathbf{u}} = 0, \quad (17)$$

with

$$\langle \hat{u}_{\text{slip}} \rangle = \frac{\hat{\omega}}{2\pi} \int_0^{2\pi/\hat{\omega}} \hat{u}_{\text{slip}} d\hat{t}, \quad \hat{u}_{\text{slip}} = -2 \sinh^{-1} \left(\frac{\hat{q}}{2(1+\delta)} \right) \frac{\partial \hat{\phi}}{\partial \hat{x}}. \quad (18)$$

The nondimensional governing equations and boundary conditions are shown schematically in Fig. 3.

3.2 Simulations

The finite-element package COMSOL Multiphysics 4.2a (COMSOL Inc., Sweden) is utilized for numerical simulation of the electro-kinetics and the flow fields (Olesen et al. 2006; Storey et al. 2006; Soni et al. 2007; Gregersen et al. 2009). For given parameter settings, simulations exploit the one-way coupling between electro-kinetic and flow dynamics, and have been carried out in two steps. Firstly, the electrostatics equation (Eq. 12) incorporating the Neumann boundary conditions (Eqs. 13 and 14) was solved in combination with the potential drop equation (Eq. 16). The time-dependent slip velocity (Eq. 18) is subsequently evaluated from the resolved electric field. Secondly, the flow field is solved for the steady Stokes equations in which the evaluated time-averaged slip velocity is applied as a boundary condition on the electrodes.

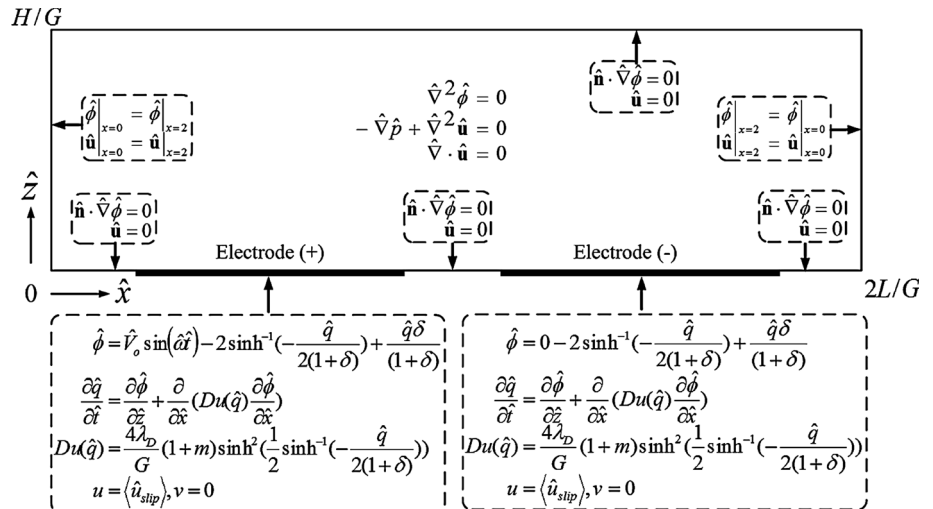
As the Neumann boundary conditions (Eq. 13 and 14) are discontinuous on the bottom of the numerical domain, the smoothed Heaviside function was adopted for a gradual transition in boundary conditions between electrodes and gaps (Speetjens et al. 2011). This method ensures convergence and thereby accurate resolution. As a result, the boundary conditions (Eqs. 13 and 14) on the bottom wall $\hat{z} = 0$ are combined as

$$\frac{\partial \hat{\phi}}{\partial \hat{z}} = [\mathcal{F}_1(\hat{x}) + \mathcal{F}_2(\hat{x})] \left[\frac{\partial \hat{q}}{\partial \hat{t}} - \frac{\partial}{\partial \hat{x}} \left(Du \frac{\partial \hat{\phi}}{\partial \hat{x}} \right) \right], \quad (19)$$

where $\mathcal{F}_{1,2} = \mathcal{H}(\hat{x} - \hat{x}_A^{(1,2)}; \varepsilon_H) \mathcal{H}(\hat{x}_B^{(1,2)} - \hat{x}; \varepsilon_H)$ with $\mathcal{H}(\hat{x}, \varepsilon_H)$ the smoothed Heaviside function within a transition region of width ε_H and positions $\hat{x}_A^{(1,2)}$ and $\hat{x}_B^{(1,2)}$ are leading and trailing edges of the electrodes, respectively. The smoothed Heaviside function is given via

$$\mathcal{H}(\hat{x}, \varepsilon_H) = [(\tanh(\hat{x}/\varepsilon_H) + 1)]/2. \quad (20)$$

Fig. 3 Dimensionless governing equations and boundary conditions



The smoothed Heaviside function attains a smooth transition from electrode to gap within a narrow region of ε_H . However, this method artificially changes the physical boundary conditions. By choosing a very small value of ε_H , the resulting error on the solution can be considered to be negligible. In this study, $\varepsilon_H = 0.05$ was used.

The geometry for the electro-kinetic and flow problems is discretized with a nonequidistant mesh so as to enhance computational accuracy and efficiency. Lagrange cubic shape functions are used in COMSOL. To ensure sufficient spatial resolution in solving Eq. 19, at least 1,000 nodes are used on the bottom of the domain and the corresponding spacing is $\Delta\hat{x} = 0.01$. This mesh meets the resolution criterion on the smoothed Heaviside function, $\Delta\hat{x} \ll \varepsilon_H$. If increasing the spatial resolution from 1,000 to 2,000 nodes, the change of $\hat{\phi}$ is less than 0.1 % for $\hat{V}_o = 10$.

4 Results and discussion

4.1 Numerical slip velocity

In order to evaluate the performance of the present numerical scheme, we compared our results with the classical GCS model used in prior work (Olesen et al. 2006). It must be noted that in the limit of very small Du number, $Du = 0$, in Eq. 14, the present model reduces to the standard GCS mode. Figure 4 shows the predicted time-averaged slip velocity profile $\langle u_{slip} \rangle$ at frequencies of 100 and 1,000 Hz for voltages of 0.5 and 2 V. The case without the effect of surface conduction ($Du = 0$) is also plotted for comparison. The profiles nicely expose the significant decline of the slip velocity nearby the electrode edge due to the surface conduction. Even though at the low applied

voltage, the effect of the surface conduction on the slip velocity is so obvious that the surface conduction cannot be neglected, which significantly reduces the slip velocity (Fig. 4a, b). When voltage increases from 0.5 to 2 V at 100 Hz, the slip velocity close to the edge is significantly reduced by a factor of about 4, and the sharp increase in the velocity near the electrode becomes spread out (Fig. 4c, d). Compared with the case in the absence of the surface conduction, the reduction in the velocity due to the surface conduction can be found nearby the center of the electrode. In addition, due to the spatial periodicity of geometry and boundary conditions, the slip velocity and the resulting entire flow field can be seen to be periodic with a periodic distance of L along the x -axis, and furthermore is symmetric relative to the center of the electrode (Ramos et al. 2003). The numerical results reveal that the surface conduction does not affect these periodicity and symmetry characteristics (Fig. 4).

However, if increasing the frequency, the reduction in the slip velocity due to the surface conduction becomes weak. To evaluate the effect surface conduction as function of frequency, a space-averaged Dukhin number along the electrode surface, $\overline{Du} = \int_0^{\hat{W}} Du(\hat{x})d\hat{x}/\hat{W}$, is calculated. Figure 5 shows \overline{Du} as a function of time over one period of the oscillation at 100 and 1,000 Hz for 2 V. The maximum of \overline{Du} at 100 Hz is up to about 1.04 while it is reduced to about 0.14 at 1,000 Hz, one order smaller than at 100 Hz. It suggests the Du number decreases with the increase in the frequency. This reduction in the Du number against the frequency is attributed to the charging procedure of the double layer. For low frequencies, the ions have sufficient time to reach the electrodes and generates a high ζ , leaving a high Du number in the double layer while for high frequency, the Du number is small due to a low ζ .

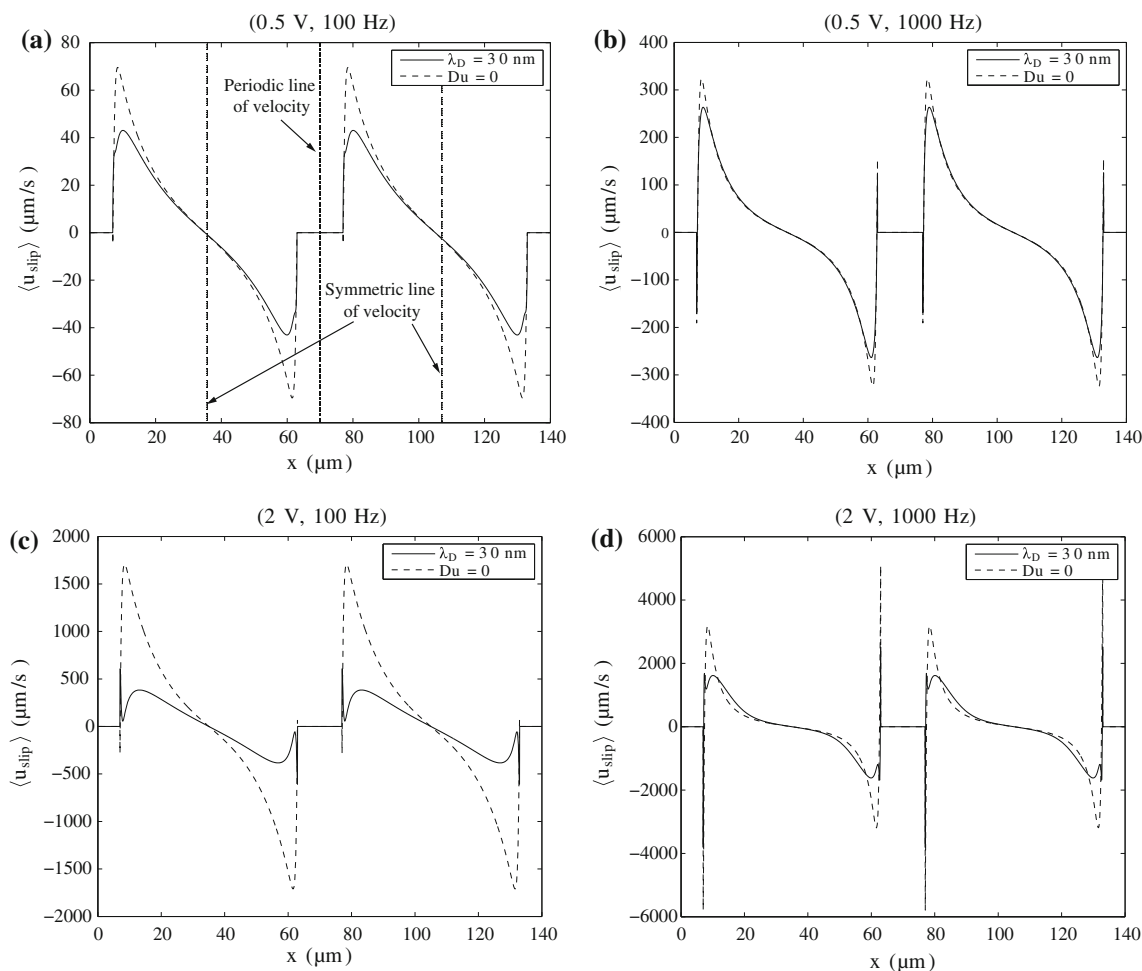


Fig. 4 Time-averaged slip velocity profiles $\langle u_{\text{slip}} \rangle$ across the electrodes at two frequencies of 100 and 1,000 Hz for two voltages, 0.5 and 2 V

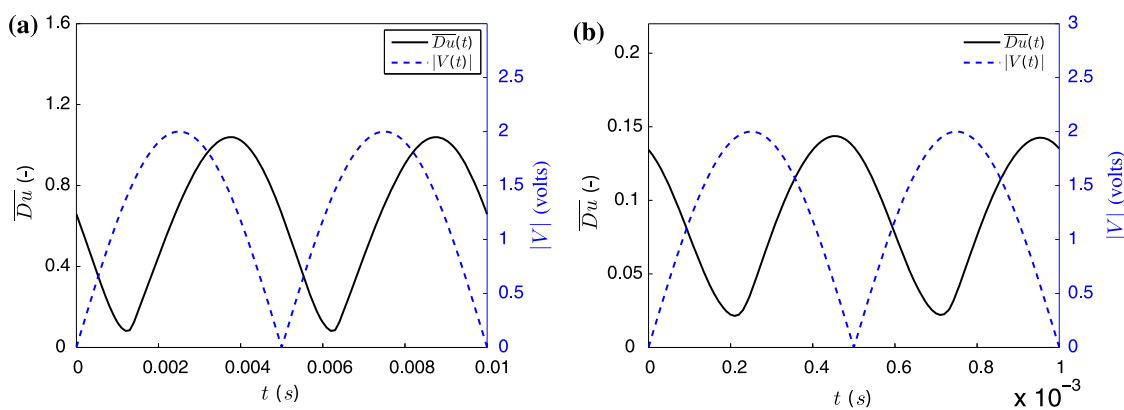


Fig. 5 Mean Du number over one period of the oscillation compared with applied voltage at 100 Hz (a) and 1,000 Hz (b) for 2 V

4.2 Comparison between numerical and experimental results

Figure 6 shows the numerical and experimental velocity vectors on an equidistant grid in the domain $0 \leq x \leq 35 \mu\text{m}$

and $3 \mu\text{m} \leq z \leq 47 \mu\text{m}$, including one half of the electrode, at a voltage of 1 V and a frequency of 1,000 Hz. The black line at the substrate indicates one half of electrode, and the x -component of velocity is indicated by the color bar. Comparing the predicted velocity field to the experimental one, it

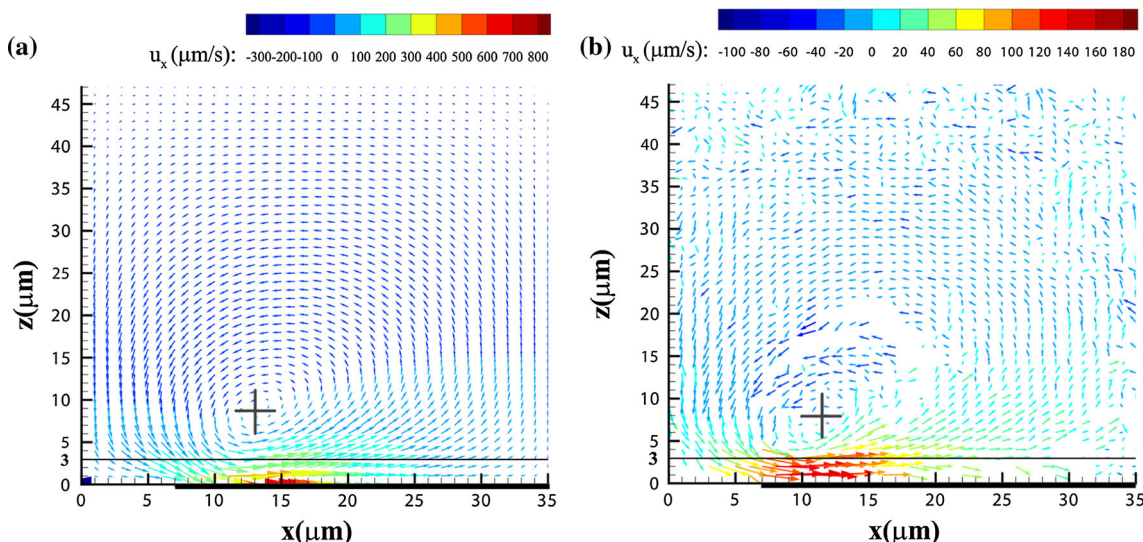


Fig. 6 Comparison of the velocity vectors between the numerical simulation and experimental result at a voltage of 1 V and a frequency of 1,000 Hz. **a** Numerical predicted velocity vectors of ACEO flow on an equidistant grid with $(\Delta x, \Delta z) = (1 \mu\text{m}, 1 \mu\text{m})$ in the domain

reveals that the numerical simulation predicts well the size and shape of the ACEO vortex and the position of the center from the experimental observation. However, the magnitude of the predicted velocity is much bigger than the experimental result.

To analyze how much deviation exists from the experimental velocities, a coefficient of deviation is defined as:

$$\theta_{\text{Dev}} = \frac{\sqrt{\frac{1}{N} \sum_{\Omega} (U_{ij}^{\text{num}} - U_{ij}^{\text{exp}})^2}}{\frac{1}{N} \sum_{\Omega} U_{ij}^{\text{exp}}} \quad (21)$$

where $U = \sqrt{u_x^2 + u_z^2}$ is the velocity magnitude, the superscripts num and exp refer to the numerical and experimental values and N is the number of velocities in the area of evaluation Ω . As a large fluctuation of the measured velocity was found close to the top wall of the channel (see Fig. 6b), the domain $0 \leq x \leq 35 \mu\text{m}$ and $3 \mu\text{m} \leq z \leq 30 \mu\text{m}$ is chosen in the evaluation of the deviation. For 1,000 Hz at 1 V, θ_{Dev} is up to 2.06.

The numerical and experimental axial velocity value above the electrodes are in detail compared, as the movement of the tracer particle with a diameter of $2 \mu\text{m}$ could be affected by the interaction between the particles and wall. Besides, the sticking particles at the wall may locally influence the electric and flow fields. Therefore, the axial velocity measured at $z \geq 3 \mu\text{m}$ is used to validate the numerical results. Figure 7 shows the numerical and experimental velocities at a voltage of 1 V and frequencies of 100 and 1,000 Hz respectively at $z = 3 \mu\text{m}$. The distribution of predicted velocity at 100 Hz is smoother along

the surface of electrodes than at 1,000 Hz. This smoother velocity field is due to the EDL fully charged in the simulation, yielding a larger Du number. For 100 Hz at 1 V, the maximum of \overline{Du} is about 0.40, compared with $\overline{Du} = 0.06$ at 1,000 Hz. In addition, the axial predicted velocities as a function of the vertical distance away from the substrate are plotted in Fig. 7. It reveals that the numerical axial velocity decreases significantly as z increases and the curvature of the velocity profile reduces along the surface as well. At a distance of $3 \mu\text{m}$ away, the curvature of the predicted velocity profile is in good agreement with the measured one.

To quantitatively match the experimental results, a correction factor A is performed on the numerical velocity. To this end, the deviation of velocity between the corrected numerical and experimental results at $z = 3 \mu\text{m}$ is calculated in terms of A as

$$\text{Dev}(A) = \sqrt{\sum_{i=0}^N [(Au_x^{\text{num}}(x_i, 3) - u_x^{\text{exp}}(x_i, 3))^2 + (Au_z^{\text{num}}(x_i, 3) - u_z^{\text{exp}}(x_i, 3))^2]} \quad (22)$$

By the minimum value of Dev, one can find the value of A , which yields the closest match between numerical and experimental results. Figure 8 shows the corrected numerical velocity and experimental one at 100 and 1,000 Hz for 1 V. Compared with $A = 0.85$ at 100 Hz, the correction factor decreases to $A = 0.38$ as the frequency increases to 1,000 Hz. The correction factor closer to the

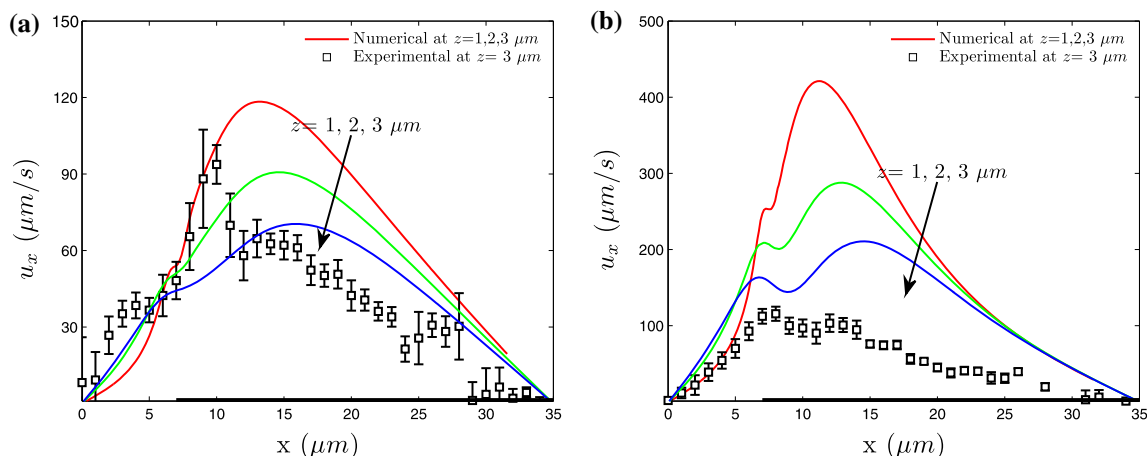


Fig. 7 Numerical and experimental velocity profiles above the electrode surface at 1 V and frequencies: **a** for 100 Hz and **b** for 1,000 Hz respectively. The *black solid line* indicates the position of the electrodes

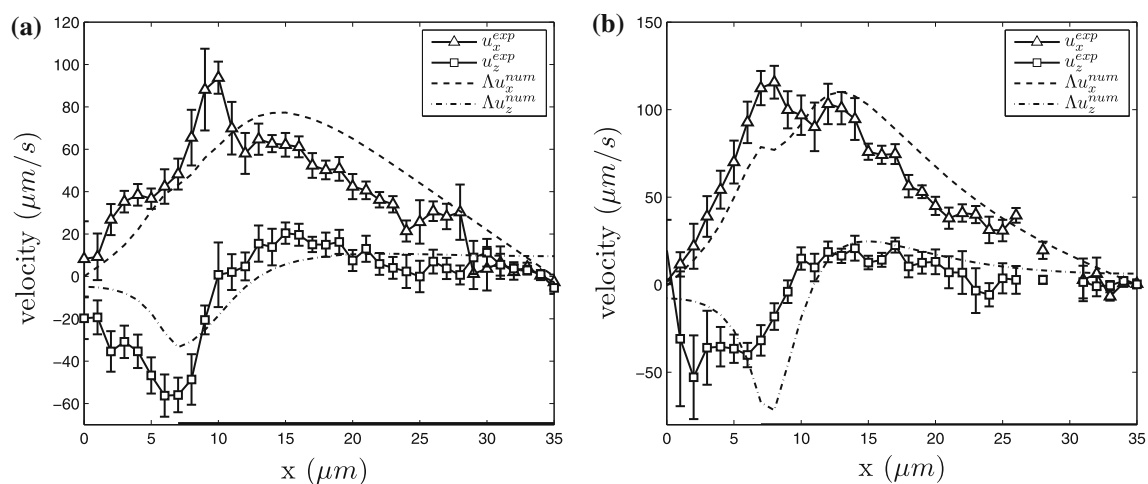


Fig. 8 Comparison between corrected numerical and experimental velocity profiles above the electrode surface at 1 V and frequencies: **a** for 100 Hz ($A = 0.85$) and **b** for 1,000 Hz ($A = 0.38$), respectively

unity at a low frequency indicates that the numerical prediction quantitatively matches the experimental velocity. As mentioned above, at a lower frequency the surface conduction becomes important. The surface conduction lowers the predicted velocity, leading to that the difference with the experimental measurement declines. Both experimental observations provide first indications that the surface conduction indeed becomes a relevant factor in the process.

Figure 9 shows the correction factor as a function of frequency for 0.5, 1, 1.5 and 2 V. At frequencies higher than 200 Hz, the correction factor may be reasonably approximated by a constant $A = 0.35$ for voltages of 0.5, 1, 1.5 and 2 V. This factor is closer to the ideal correction factor $A = 1$ than the factor $A = 0.25$ found in Green et al. (2002), signifying a better prediction by the nonlinear model compared with the linear model of Green et al.

(2002). However, the improvement is modest, since the departure of A from unity is still significant.

Adopting the Green's method, in the present simulation at frequencies higher than 200 Hz, we introduce a correction factor $A = 0.35$ in the Helmholtz–Smoluchowski formula (Eq. 10) as follows (Green et al. 2000, 2002; Bazant et al. 2009):

$$u_{\text{slip}}^* = -A \frac{\varepsilon \zeta}{\mu} E_T. \quad (23)$$

4.3 Vortex structure

According to the velocity field, one can calculate the spanwise component of the vorticity by $\omega_y = \partial u_x / \partial z - \partial u_z / \partial x$. In this study, due to the large fluctuation of the measured velocity, the interpolated velocity field is further smoothed

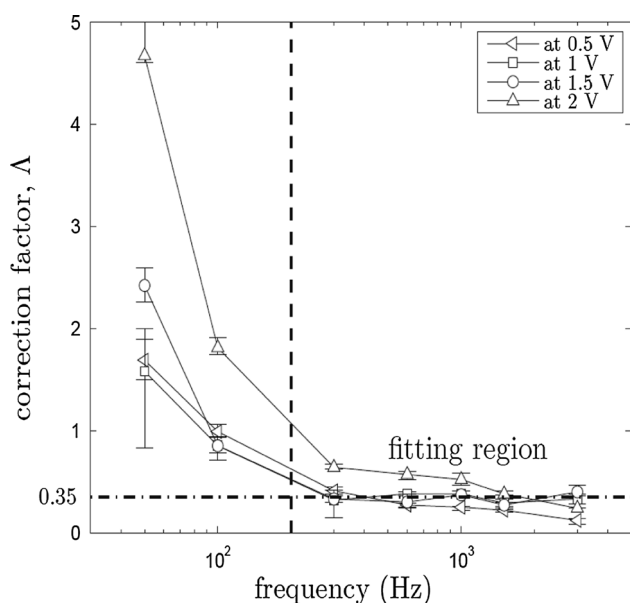


Fig. 9 Correction factor as a function of frequency

by a combination of discrete cosine transforms and a penalized least-squares approach (Garcia 2011). Figure 10 shows the comparison of the spanwise component of its vorticity between the corrected numerical prediction ($\Lambda = 0.35$) and the experimental measurement at a voltage of 1.5 V and a frequency of 1,000 Hz in the domain for which $0 \leq x \leq 35 \mu\text{m}$ and $3 \mu\text{m} \leq z \leq 47 \mu\text{m}$. The circulation, i.e., strength, of the vortex is given via the area integral, $\Gamma = \int_A \omega_y dA$, where the area A is determined via eigenvalues of the strain-rate tensor (λ_2 -method) (Jeong and Hussain 1995; Vollmers 2001). It exhibits that the area A of the vorticity obtained in the experiment is consistent with the prediction, and its circulation ($2,416.0 \mu\text{m}^2/\text{s}$) is in good agreement with the numerical result ($2,209.9 \mu\text{m}^2/\text{s}$). Its vortex center ($x_c = \frac{1}{\Gamma} \int_A \omega_y x dA, z_c = \frac{1}{\Gamma} \int_A \omega_y z dA$) is at a distance of about $4.5 \mu\text{m}$ from the electrode edge and $9.3 \mu\text{m}$ from the substrate, which is similar to the prediction where a distance of $5.8 \mu\text{m}$ from the edge and $7.9 \mu\text{m}$ from the substrate is found.

Figure 11 shows the comparison between the experimental and numerical circulations (with $\Lambda = 0.35$ when frequencies higher than 200 Hz) as a function of frequency at voltage of 1, 1.5 and 2 V. It reveals that the experimental circulation Γ is dependent on the frequency, where the frequency at which the maximum occurs is 600 Hz at 1 V and reduces to 300 Hz as the voltage increases to 2 V. As the magnitude of Γ is directly related to the velocity field, and the velocity field is induced by the slip velocity of ACEO, the dependence of Γ on the frequency can be considered to reflect the characteristics of the slip velocity on the frequency. The results on the maximum of the

circulation (at 600 Hz at 1 V and at 300 Hz at 2 V) is consistent with the maximum velocity and thus occurs near the so-called characteristic frequency of the velocity (Ramos et al. 2003; Olesen et al. 2006). Such a shift of the characteristic frequency with voltage is due to the nonlinear charging procedure in the double layer (Olesen et al. 2006). With the increase in the voltage, the RC time for charging the double layer through the bulk electrolyte significantly increases due to the nonlinear increase in double layer capacitance. Consequently, the characteristic frequency of the slip velocity is reduced by the increase in voltage. The numerical prediction on maximum of Γ with $\Lambda = 0.35$ is about 600 and 500 Hz for 1 and 2 V, respectively (see Fig. 11), which is similar to the experimental observation. It demonstrates that the numerical nonlinear model correctly predicts the tendency of the frequency dependence for ACEO flow obtained in the experiments.

4.4 Discussion of the results

For quantification of the effect of the correction factor on the prediction of the ACEO flow at frequencies higher than 200 Hz, the velocity deviation in terms of $u_x^{\text{num}} - u_x^{\text{exp}}$ and $u_z^{\text{num}} - u_z^{\text{exp}}$ (u^{num} is the corrected numerical velocity with $\Lambda = 0.35$) at 1 V and 1,000 Hz is shown in Fig. 12a, where the absolute value of the deviation of the velocity magnitude ($|U^{\text{num}} - U^{\text{exp}}|$) is indicated in colors. It shows that relative large deviations occur primarily near the electrode edge. This could be caused by dielectrophoresis. Close to the electrode edge, the dielectrophoresis reaches a maximum, acting toward the electrode edge due to $Re(\chi_{\text{CM}}) > 0$ (Green and Morgan 1999). As expected, the direction of the deviations in Fig. 12a is consistent with the direction of the DEP (toward the electrode edge), indicating that the dielectrophoresis could be an important reason of the deviations.

Figure 12b shows a coefficient of deviation θ_{Dev} (see Eq. 21) as function of frequency at voltages from 0.5 to 2 V. For frequencies higher than 200 Hz with $\Lambda = 0.35$, the coefficient of the deviation reduces to about a value of 0.5, indicating that the corrected numerical prediction quantitatively matches the measured velocity field with a relative low variation. And as expected, a relative low coefficient of deviation is also found at low frequency and high voltage with $\Lambda = 1$, where higher surface conduction lowers the ACEO velocity to be comparable with the numerical prediction. Additionally, as a high local deviation near the electrode edges exists and its effect could arise from the DEP, the coefficient of the deviations is shown as function of the voltage. At a frequency higher than 200 Hz, when the voltage changing from 1 to 2 V, θ_{Dev} increases from approximately 0.36 to 0.50 (Fig. 9). Its tendency as

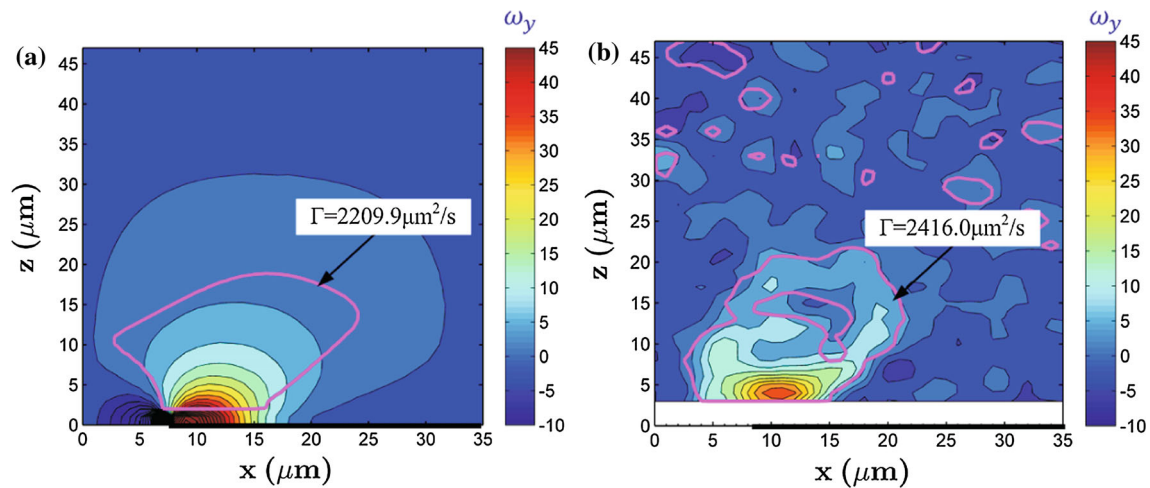


Fig. 10 Vorticity and circulation at 1.5 V and frequency of 1,000 Hz, where the *red solid line* indicates the boundary of the ACEO vortex, $\lambda_2 = -10$. **a** Corrected prediction ($A = 0.35$), **b** experimental results (color figure online)

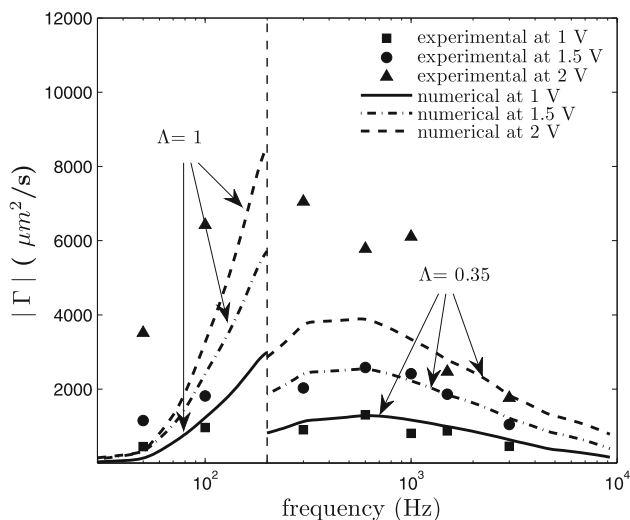


Fig. 11 Comparison between the experimental and numerical circulations with $A = 0.35$ as a function of frequency at voltages of 1, 1.5 and 2 V

function of voltage is consistent with the dielectrophoresis. The deviation at 2 V (compared to 1–1.5 V) is expected due to nonlinear effects. To reduce the DEP effect, further studies should focus on improving the optical system to allow for smaller tracer particles in the measurements.

In the present numerical study, the classical GCS model was used to simulate the ACEO slip velocity by simultaneously accounting for the surface conduction. Some limitations of the used GCS model are that the molecular nature of the solvent is neglected, and as a consequence, in the double layer the relative permittivity is taken as a constant. In a recent study by Das et al. (2012), the field-dependent solvent polarization, like for water dipoles, is taken into account. As the polar solvent molecules get

oriented, in response to the electric field in the EDL, the permittivity of the solvent will be field dependent and may be considerably reduced in comparison with the bulk properties. Due to that the EDL potential gradient and thickness decrease as well. This effect is most prominent for larger values of wall potential and solvent polarization A . For a 10-nm-thick water channel, a value is found of $A = 0.1$, while in our case a much lower value of 10^{-5} is found. So for microchannels and relatively low potential values, the assumption made of constant relative permittivity seems reasonable.

Faradaic current injection can also become more dominant at high frequencies and voltages. The study by Olesen et al. (2006) on a comparable system reveals that Faradaic current injection becomes significant for higher frequencies, manifesting itself in a decreasing slip velocity and at some point even in flow reversal. This suggests an overall larger deviation between experiments and simulations in the higher frequency regime. This trend is consistent with the behavior found in our system in that the correction factor A progressively drops below unity (signifying stronger overprediction by the model) for frequencies beyond approximately 200 Hz (Fig. 9). This identifies Faradaic current injection as a potential factor in at least this regime. However, for lower frequencies (below 200 Hz), the opposite happens; the model underpredicts the experimental results ($A > 1$). This signifies a change in relative contribution of the electro-kinetic mechanisms acting near the electrodes, yet it is unclear how. Increasing the voltage overall tends to amplify the slip velocity. Though not yet understood, the nonlinear nature of both current injection and surface conduction as well as their interplay is believed primary causes. Nonlinear current injection has in Olesen et al. (2006), e.g., been observed to promote higher slip velocities at lower frequencies; increasing the voltage amplifies this effect

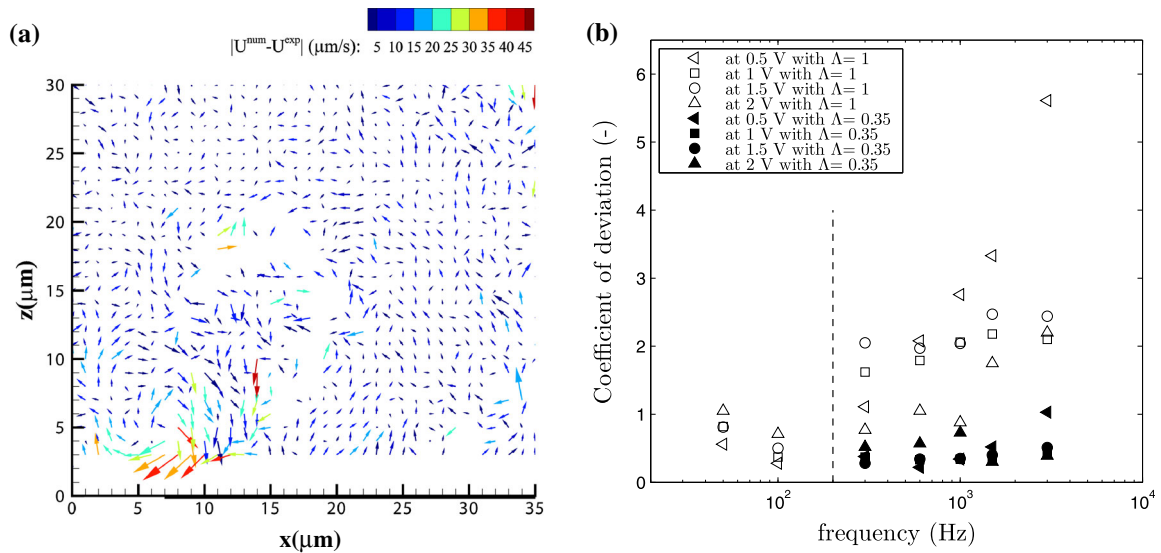


Fig. 12 **a** Deviation of the velocity magnitude of the flow fields between the corrected prediction ($\Lambda = 0.35$) and experiments at 1 V and 1,000 Hz, where the vectors are given by $(u_x^{\text{num}} - u_x^{\text{exp}})$ and

$(u_z^{\text{num}} - u_z^{\text{exp}})$ at $0 \leq x \leq 35 \mu\text{m}$ and $3 \mu\text{m} \leq z \leq 30 \mu\text{m}$. **b** Coefficient of deviation as a function of frequency

up to a certain threshold, beyond which it again diminishes. This reasonably correlates with our observations at lower frequencies in that the correction factor increases substantially in this regime.

5 Conclusions

In this paper, we present an experimental investigation to validate the numerical prediction on the vortical structures due to AC electro-osmosis. The 3D fluid velocities above the symmetric electrodes are obtained using astigmatism μ -PTV and used to validate the numerical prediction in an extended nonlinear GCS model accounting for surface conduction effects. It reveals that the surface conduction in the present model reduces the over-prediction of GCS model as clearly visible at lower frequency and high voltage in the experiments. The structure and position of the ACEO vortex are qualitatively in good correspondence with the experiments. The curvature of predicted axial velocity value is in good agreement with the measured at a distance of 3 μm above the electrode surface. At a higher frequency, a higher predicted velocity is observed compared with the experiments. A correction factor has been estimated to be $\Lambda = 0.35$ in the frequency range of 200–3,000 Hz and at voltages of 0.5, 1, 1.5 and 2 V. This value is larger than the factor $\Lambda = 0.25$ in Green’s work at 0.5 V (Green et al. 2002), signifying a better prediction by the nonlinear model comparable to the linear model adopted in Green et al. (2002). After using a velocity field correction factor, the coefficient of deviation reduces to approximately 0.5 at 0.5, 1, 1.5 and 2 V. The relative low

correspondence between the simulation and measurement after correction may possibly result from the dielectrophoretic effect on the movement of the tracing particles near the electrode edge in the experiment, especially at low frequencies. At high frequencies, the deviations are most likely related to Faradaic current injection.

The circulation has been quantified as a function of frequency. It shows that the maximum of experimental circulation is at 600 Hz for 1 V and at 300 Hz for 2 V, and the circulation becomes smaller when the frequency is high or low. This frequency shift of the maximum is captured in the simulation. It signifies that the present numerical model correctly predicts the qualitative frequency and voltage dependence for ACEO flow obtained in the experiments. Further development of the present model will be needed to fully describe the experimental results, including other factors, e.g., the influence of DEP and the Faradaic current injection. This work may contribute to further understanding of ACEO flow and explanation of some of the phenomena observed in experiments.

References

Ajdari A (2000) Pumping liquids using asymmetric electrode arrays. *Phys Rev E* 61:R45–R48
 Bazant MZ, Kilic MS, Storey BD, Ajdari A (2009) Towards an understanding of induced-charge electrokinetics at large applied voltages in concentrated solutions. *Adv Colloid Interface Sci* 152:48–88
 Castellanos A, Ramos A, Gonzalez A, Green NG, Morgan H (2003) Electrohydrodynamics and dielectrophoresis in microsystems: scaling laws. *J Phys D* 36:2584–2597
 Chen S, Angarita-Jaimes N, Angarita-Jaimes D, Pelc B, Greenaway AH, Towers CE, Lin D, Towers DP (2009) Wavefront sensing

- for three-component three-dimensional flow velocimetry in microfluidics. *Exp Fluids* 47:849–863
- Cierpka C, Segura R, Hain R, Kähler CJ (2010) A simple single camera 3C3D velocity measurement technique without errors due to depth of correlation and spatial averaging for microfluidics. *Meas Sci Technol* 21:045401
- Cierpka C, Rossi M, Segura R, Kähler CJ (2010) On the calibration of astigmatism particle tracking velocimetry for microflows. *Meas Sci Technol* 22:015401
- Das S, Chakraborty S, Mitra SK (2012) Redefining electrical double layer thickness in narrow confinements: effect of solvent polarization. *Phys Rev E* 85:051508
- Garcia D (2011) A fast all-in-one method for automated post-processing of PIV data. *Exp Fluids* 50:1247–1259
- Green NG, Morgan H (1999) Dielectrophoresis of submicrometer latex spheres. I. Experimental results. *J Phys Chem B* 103(1):41–50
- Green NG, Ramos A, Gonzalez A, Morgan H, Castellanos A (2000) Fluid flow induced by nonuniform ac electric fields in electrolytes on microelectrodes. I. Experimental measurements. *Phys Rev E* 61:40114018
- Green NG, Ramos A, Gonzalez A, Morgan H, Castellanos A (2002) Fluid flow induced by nonuniform ac electric fields in electrolytes on microelectrodes. III. Observation of streamlines and numerical simulation. *Phys Rev E* 66:026305
- Gregersen MM, Andersen MB, Soni G, Meinhart C, Bruus H (2009) Numerical analysis of finite Debye-length effects in induced-charge electro-osmosis. *Phys Rev E* 79:066316
- Jeong J, Hussain F (1995) On the identification of a vortex. *J Fluid Mech* 285:69–94
- Khair AS, Squires TM (2008) Surprising consequences of ion conservation in electro-osmosis over a surface charge discontinuity. *J Fluid Mech* 615:323–334
- Kilic MS, Bazant MZ, Ajdari A (2007) Steric effects in the dynamics of electrolytes at large applied voltages. II. Modified Poisson–Nernst–Planck equations. *Phys Rev E* 75:021503
- Kim BJ, Yoon SY, Lee KH, Sung HJ (2009) Development of a microfluidic device for simultaneous mixing and pumping. *Exp Fluids* 46:85–95
- Liu Z, Speetjens MFM, Frijns AJH, van Steenhoven AA (2014) Application of astigmatism μ -PTV to analyze the vortex structure of AC electroosmotic flows. *Microfluid Nanofluid* 16:553–569. doi:10.1007/s10404-013-1253-2
- Lyklema J (1995) Solid–liquid interfaces, Vol. II of Fundamentals of interface and colloid science. Academic Press, San Diego
- Morgan H, Green NG (2002) AC electrokinetic: colloids and nanoparticles. Research Studies Press, Hertfordshire
- Olesen LH, Bruus H, Ajdari A (2006) AC electrokinetic micropumps: the effect of geometrical confinement, faradaic current injection, and nonlinear surface capacitance. *Phys Rev E* 73:056313
- Ramos A, Morgan H, Green NG, Castellanos A (1998) AC electrokinetics: a review of forces in microelectrode structures. *J Phys D Apply Phys* 31:2338–2353
- Ramos A, Morgan H, Green NG, Castellanos A (1999) AC electric field-induced fluid flow in microelectrodes. *J Colloid Interface Sci* 217:420–422
- Ramos A, Gonzalez A, Castellanos A, Green NG, Morgan H (2003) Pumping of liquid with ac voltage applied to asymmetric pairs of microelectrodes. *Phys Rev E* 67:056302
- Soni G, Squires TM, Meinhart CD (2007) Nonlinear phenomena in induced charge electroosmosis. In: 2007 ASME international mechanical engineering congress and exposition, Seattle, USA
- Speetjens MFM, Wispelaeere HNL, van Steenhoven AA (2011) Multi-functional Lagrangian flow structures in three-dimensional ac electro-osmotic micro-flows. *Fluid Dyn Res* 43:035503
- Storey BD, Edwards LR, Kilic MS, Bazant MZ (2006) Steric effects on ac electro-osmosis in dilute electrolytes. *Phys Rev E* 77:036317
- Vollmers H (2001) Detection of vortices and quantitative evaluation of their main parameters from experimental velocity data. *Meas Sci Technol* 12:1199–1207